



Cite this: *Phys. Chem. Chem. Phys.*,  
2018, 20, 5644

# Low energy electron-induced decomposition of $(\eta^5\text{-Cp})\text{Fe}(\text{CO})_2\text{Mn}(\text{CO})_5$ , a potential bimetallic precursor for focused electron beam induced deposition of alloy structures†

Rachel M. Thorman,<sup>a</sup> Ilyas Unlu,<sup>b</sup> Kelsea Johnson,<sup>c</sup> Ragnar Bjornsson,<sup>id</sup><sup>a</sup>  
Lisa McElwee-White,<sup>id</sup><sup>c</sup> D. Howard Fairbrother,<sup>id</sup><sup>b</sup> and Oddur Ingólfsson,<sup>id</sup><sup>\*a</sup>

The production of alloyed nanostructures presents a unique problem in focused electron beam induced deposition (FEBID). Deposition of such structures has historically involved the mixing of two or more precursor gases *in situ* or *via* multiple channel gas injection systems, thereby making the production of precise, reproducible alloy compositions difficult. Promising recent efforts to address this problem have involved the use of multi-centred, heterometallic FEBID precursor species. In this vein, we present here a study of low-energy electron interactions with cyclopentadienyl iron dicarbonyl manganese pentacarbonyl ( $(\eta^5\text{-Cp})\text{Fe}(\text{CO})_2\text{Mn}(\text{CO})_5$ ), a bimetallic species with a polyhaptic ligand (Cp) and seven terminal carbonyl ligands. Gas phase studies and coupled cluster calculations of observed low-energy electron-induced reactions were conducted in order to predict the performance of this precursor in FEBID. In dissociative electron attachment, we find single CO loss and cleavage of the Fe–Mn bond, leading to the formation of  $[\text{Mn}(\text{CO})_5]^-$ , to be the two dominant channels. Contributions through further CO loss from the intact core and the formation of  $[\text{Mn}(\text{CO})_4]^-$  are minor channels. In dissociative ionization (DI), the fragmentation is significantly more extensive and the DI spectra are dominated by fragments formed through the loss of 5 and 6 CO ligands, and fragments formed through cleavage of the Fe–Mn bond accompanied by substantial CO loss. The gas phase fragmentation channels observed are discussed in relation to the underlying processes and their energetics, and in context to related surface studies and the likely performance of this precursor in FEBID.

Received 29th September 2017,  
Accepted 23rd January 2018

DOI: 10.1039/c7cp06705d

rsc.li/pccp

## 1 Introduction

The fabrication of magnetic nanostructures has become increasingly vital to many emergent fields both in academic research and industry, including information technology, nanoelectronics, and spintronics.<sup>1,2</sup> Currently, such nanostructures are commonly manufactured *via* the top-down approach ubiquitous in nanolithography – optical lithography has produced nanostructures as small as 22 nm, while ion milling has produced structures as small as 10 nm.<sup>1</sup> Despite these advances, there are clear drawbacks to these techniques. Optical lithography is a multistep process and each step has the potential to degrade the quality of the produced structure, which may affect device functionality; this is of particular concern at the nanoscale.<sup>1,2</sup> Additionally, expensive masks must be produced for use in photolithography, which are often themselves degraded by the lithography process.

Ion milling, despite its improved lateral resolution, has the potential effect of ion implantation, which may affect the magnetic properties of the materials used.<sup>1,3</sup>

Focused electron beam induced deposition (FEBID),<sup>4,5</sup> conversely, is a single-step, bottom-up process wherein nanostructures can be directly written onto three-dimensional surfaces. In FEBID, electron-driven reactions are used to deposit pure metal nanostructures onto surfaces. In a high-vacuum instrument equipped with a tightly-focused electron beam (*e.g.* an SEM or TEM), a substrate is exposed to a constant flux of organometallic precursors. Ideally, electron-driven reactions will cause the metal centres of these precursors to deposit onto the substrate under the area of the primary electron beam, while the organic ligands fully dissociate and are pumped away. The electron beam can then be rastered around the surface, allowing it to deposit any lateral geometry, while the vertical dimension of the deposit may be controlled through variations in dwell time. FEBID has been used to deposit nanowires, nanosprings and nanodots, as well as many other structures.<sup>1,4,5</sup> High resolution capacity has been demonstrated through production of nanodots as small as 0.7 nm, as well as lines with a width of 1.9 nm

<sup>a</sup> Science Institute and Department of Chemistry, University of Iceland, Reykjavik, Iceland. E-mail: odduring@hi.is; Fax: +354 552-8911; Tel: +354 525-4313

<sup>b</sup> Department of Chemistry, Johns Hopkins University, Baltimore, Maryland, USA

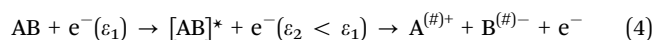
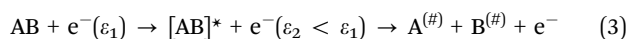
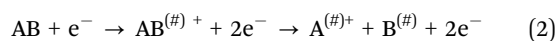
<sup>c</sup> Department of Chemistry, University of Florida, Gainesville, Florida, USA

† Electronic supplementary information (ESI) available. See DOI: 10.1039/c7cp06705d

and a spacing of 3.2 nm.<sup>6</sup> High purity nanostructures,<sup>4,7</sup> including magnetic nanostructures,<sup>1,7–10</sup> have also been produced with FEBID. Furthermore, though FEBID does currently not have the same capacity for high industrial throughput as do photolithographic techniques, it has been used successfully for research and prototyping.<sup>4</sup>

However, although FEBID has been used to deposit nanostructures with high lateral resolution and high purity, this is not routinely achieved. Presently, the two major challenges facing FEBID are (i) deposit contamination as a result of incomplete ligand dissociation and (ii) deposit broadening outside the area of the primary electron beam. This is in part due to suboptimal precursor chemistry and appropriate precursors must be designed in order to address these challenges. In order to design such optimal precursors, it is important to understand the electron-driven processes by which deposits are formed from precursors on surfaces. Low-energy electrons (commonly defined as electrons below 100 eV in energy) are abundant on surfaces during FEBID experiments. The energy distribution of secondary and backscattered electrons on surfaces irradiated with a high-energy primary electron beam generally reaches its peak well below 10 eV, and such electrons are scattered within an area several times as large as the area of the primary electron beam.<sup>4,5,11–15</sup> Low-energy electrons are additionally known to react with FEBID precursors to produce incomplete ligand dissociation, and have previously been found to be important in the deposition of materials from various precursors.<sup>11,16–23</sup>

There are four major reaction pathways initiated by low-energy electrons: Dissociative Electron Attachment (DEA), Dissociative Ionization (DI), Neutral Dissociation (ND) and Dipolar Dissociation (DD).<sup>11,24–30</sup> These reactions are initiated by electrons of very different energies and produce several different types of dissociation products. The respective reaction schemes for each of these pathways are shown here:



In the above reaction pathways, # denotes species that may be in vibrationally and/or electronically excited states, \* identifies species that are in electronically excited states and  $\varepsilon_1$  and  $\varepsilon_2$  are the energy of the electron before and after the inelastic scattering event leading to ND or DD.

DEA (1) is a resonant process wherein a molecule captures a low energy electron, in essentially a vertical transition from the neutral molecule's ground state to the ground state or other accessible excited states of the anion (see *e.g.* ref. Bald *et al.*,<sup>25</sup> Fabrikant *et al.*<sup>30</sup> and references therein). This forms a transient negative ion (TNI), which then relaxes, either by emitting the electron in a process called autodetachment or by dissociation, leading to the formation of a negative ion fragment and one or more neutral fragments. The DEA process is generally confined to a narrow energy range below the ionization threshold of the

molecule, usually 0–10 eV, and is most efficient at around 0 eV. The high efficiency close to 0 eV is due to the cross section for electron attachment at very low energies being proportional to  $E^{-0.5}$ ,<sup>31</sup> allowing sufficient time for dissociation.<sup>30</sup> We note, however, that recent gas phase studies have been performed on an exceptional molecule, HFeCo<sub>3</sub>(CO)<sub>12</sub>, showing DEA more than 11 eV above its ionization threshold (at above 20 eV!).<sup>32,33</sup>

Unlike DEA, DI, ND and DD are all non-resonant processes,<sup>11,26,27,29</sup> showing threshold behaviour rather than resonance behaviour. In DI (2), an electron positively ionizes a molecule *via* direct impact. DI thus has an onset at or above the ionization threshold of the parent molecule. The positive parent ion, which may also be electronically or vibrationally excited, may then dissociate in order to redistribute its internal excess energy, producing a positive ion and one or more neutral fragments, generally radicals. The total cross section for DI typically increases until reaching a maximum between 50 and 100 eV, with the branching ratio shifting toward multiple bond ruptures with increasing incident electron energy. After this maximum, the total cross section decreases as energy transfer from the electron projectile to the molecular target becomes less efficient with increasing electron energy.

Neutral dissociation (3) proceeds through an electron-initiated transition of the parent molecule to electronically excited states higher in energy than the respective bond dissociation energies.<sup>34</sup> At threshold, these typically involve occupation of the lowest unoccupied antibonding orbitals; however, as the incident electron energy increases, the manifold of excited states that couple with dissociative channels also increases. In ND two or more neutral fragments are produced, most often radicals, and these fragments are commonly vibrationally or electronically excited. Dipolar dissociation (4) proceeds similarly to ND; however, it produces both an anionic fragment and a cationic fragment. It is less efficient than either DEA or DI and is likely also less efficient than ND, due to the Coulombic attraction between the product fragments. In organometallic compounds, where the first electronic excitations are at fairly low energies and the bond dissociation energy is generally low, the threshold for ND is expected to be close to 3–4 eV.

The products of each of these reaction pathways will differ significantly in their potential implications for FEBID – various positive and negative ions and radical neutrals, all of which may be in excited states, will have very different reaction profiles in FEBID and thus will initiate reactions leading to varying deposition dynamics. The secondary electron spectrum of the surface used in FEBID, in conjunction with the energy dependence and branching ratios of the individual reaction paths for the precursor molecule, will determine the importance of these channels and, ultimately, the composition of the deposits. It is thus important to understand the branching ratios of the electron-induced reactions of these precursor molecules in order to predict their viability for use in FEBID, as well as to optimize design of future FEBID precursors. Furthermore, a comparison of the observed extent and branching ratios of these different reaction channels in the gas phase, with the initial electron induced fragmentation observed when these molecules are adsorbed on surfaces, may

provide additional information on the dominant reaction pathways to be expected under actual FEBID conditions.

Compared to the deposition of pure metals, production of alloyed deposits presents additional challenges in FEBID. Deposition of alloyed nanostructures *via* FEBID has previously been performed by mixing precursor gases *in situ*, using dual or multichannel gas injection systems.<sup>1,4,35,36</sup> However, production of precise, reproducible alloy compositions remains elusive, and use of multiple precursor gases increases the potential for deposit contamination *via* incomplete ligand dissociation.<sup>37</sup> Further, it can be difficult to predict how multiple precursor gases will interact *in situ* with both one another and with the surface. To combat these issues, the use of heterometallic organometallic species has been employed. In a 2015 FEBID study, Porrati *et al.* deposited CoFe alloy nanostructures from the heteronuclear precursor  $\text{HFeCo}_3(\text{CO})_{12}$ , routinely achieving 80 at% pure metal deposits with the same stoichiometric Co : Fe ratio present in the precursor.<sup>7</sup> Gas phase studies have been performed by T. P. *et al.*<sup>32,33</sup> on this same molecule in order to elucidate its electron-induced deposition mechanisms, and seek connections to the high performance of this precursor in FEBID. This molecule was found to be susceptible to DEA at up to 20 eV incident electron energy, which is about 11 eV above its ionization threshold. This unusual behaviour has been attributed to the high density of metal-based HOMOs coming from the four metal atoms and low-energy unoccupied CO  $\pi^*$  orbitals coming from the twelve carbonyl ligands, which include both bridging and terminal carbonyls. This combination allows long-lived multi-particle-multi-hole resonances at high energies, resulting in quasi-continuous electron attachment from about 1 eV up to 20 eV. This unusual behaviour has been discussed in context to the exceptional behaviour of  $\text{HFeCo}_3(\text{CO})_{12}$  in FEBID; however, a recently published UHV surface study by T. P. *et al.*<sup>38</sup> noted that the extent of the initial fragmentation of this precursor adsorbed on a gold surface is much closer to that observed through DI in the gas phase, suggesting that the behaviour of this molecule upon electron impact may be more relevant to its excellent FEBID performance than its unusual behaviour with respect to electron attachment. A recent combined gas phase, UHV surface and FEBID study on the similar bimetallic precursor  $\text{H}_2\text{FeRu}_3(\text{CO})_{13}$  demonstrated that, despite its apparent similarity to  $\text{HFeCo}_3(\text{CO})_{12}$ ,  $\text{H}_2\text{FeRu}_3(\text{CO})_{13}$  performs sub-optimally in FEBID.<sup>39</sup> It was found to have limited reproducibility and <26 at% metal content in the deposits. The authors attribute this to a higher thermal stability of the  $\text{H}_2\text{FeRu}_3(\text{CO})_{\text{avg}=4,5}$  intermediate formed in the initial electron induced decomposition in the UHV surface experiments, as compared to the thermally labile  $\text{HFeCo}_3(\text{CO})_{\text{avg}=3}$  intermediate formed in the initial electron-induced decomposition of adsorbed  $\text{HFeCo}_3(\text{CO})_{12}$ . To our knowledge, these are the only two bimetallic precursors that have been studied to date, so there is obviously considerable work that needs to be done to further explore the potential of this strategy for the production of alloy nanostructures.

Here we present a gas phase study on dissociative electron attachment (DEA) and dissociative ionization (DI) of a similar, albeit smaller, binuclear heterometallic iron–manganese precursor:

cyclopentadienyl iron dicarbonyl manganese pentacarbonyl ( $(\eta^5\text{-Cp})\text{Fe}(\text{CO})_2\text{Mn}(\text{CO})_5$ ).<sup>40</sup> Further, in order to elucidate its gas phase behaviour upon electron interaction we use quantum chemical calculations to aid the interpretation of the observed processes. We also compare experimental results from gas phase studies with the electron-induced decomposition of this bimetallic precursor adsorbed on a solid surface. Such a comparison can provide valuable insight into the behaviour of this precursor upon electron irradiation at surfaces, which in turn may provide insight into its behaviour under FEBID conditions.

## 2 Experimental

### 2.1 Synthesis of $(\eta^5\text{-C}_5\text{H}_5)\text{Fe}(\text{CO})_2\text{Mn}(\text{CO})_5$

All reactions were carried out under an inert atmosphere using Schlenk line and glovebox techniques, unless otherwise stated.  $(\eta^5\text{-C}_5\text{H}_5)\text{Fe}(\text{CO})_2\text{I}$  and  $\text{Mn}_2(\text{CO})_{10}$  were purchased from Sigma-Aldrich and used as received. Tetrahydrofuran (THF) was distilled from sodium benzophenone ketyl and was stored over 3 Å molecular sieves prior to use. IR spectroscopy was performed on a Bruker Alpha spectrometer using a sealed KBr liquid cell from Sigma-Aldrich.

Modified literature procedures were used to synthesize  $(\eta^5\text{-C}_5\text{H}_5)\text{Fe}(\text{CO})_2\text{Mn}(\text{CO})_5$ .<sup>40</sup> A 1% Na/Hg amalgam was made by dissolving Na (0.1237 g, 5.381 mmol) in Hg (12.4140 g).  $\text{Mn}_2(\text{CO})_{10}$  (0.7690 g, 1.978 mmol) was dissolved in THF (15 mL) and added to the Na/Hg amalgam. The solution was allowed to stir for 1 hour. The organic layer was transferred to a Schlenk flask containing  $(\eta^5\text{-C}_5\text{H}_5)\text{Fe}(\text{CO})_2\text{I}$  (1.2056 g, 3.9767 mmol) and allowed to stir for 2 days, under the exclusion of light, during which time the product was formed *via* reaction (1) (see Fig. 1).

MeOH (2.0 mL) was added to the deep red solution. The solvent was removed *in vacuo* and the solid was extracted with  $\text{CH}_2\text{Cl}_2$ . After filtration, the solvent was removed under reduced pressure and column chromatography was performed on a silica column with pentane as the eluent. Three bands were seen: yellow  $\text{Mn}_2(\text{CO})_{10}$ , red product, and brown  $(\eta^5\text{-C}_5\text{H}_5)\text{Fe}(\text{CO})_2\text{I}$ , which stays on the baseline. After chromatographic separation the product was obtained as a dark red solid after sublimation at 46 °C, 100 mTorr. Crude yield: 0.5418 g, 37%. Sublimed yield: 0.2840 g, 19%. The compound was characterized by comparison to literature data.<sup>40</sup>  $^1\text{H}$  NMR (300 MHz,  $\text{C}_6\text{D}_6$ )  $\delta$  3.97 (s, 5H). IR (hexanes): 2082, 2014, 1991, 1976, 1945  $\text{cm}^{-1}$ .

### 2.2 Crossed beam gas phase studies

The crossed electron/molecular beam instrument used to measure ion yields of fragments produced *via* DEA and DI to  $(\eta^5\text{-Cp})\text{Fe}(\text{CO})_2\text{Mn}(\text{CO})_5$  in the gas phase has been previously described;<sup>41</sup> a brief description of this apparatus is provided here. The bimetallic  $(\eta^5\text{-Cp})\text{Fe}(\text{CO})_2\text{Mn}(\text{CO})_5$  precursor was



Fig. 1 Synthesis of  $(\eta^5\text{-C}_5\text{H}_5)\text{Fe}(\text{CO})_2\text{Mn}(\text{CO})_5$ .

sublimed at a temperature of 40 °C in a stainless steel gas inlet system (GIS), which was attached to a high-vacuum collision chamber. The GIS consists of a 9 mm, capped Swagelok T-fitting separated from the chamber by a variable leak valve. The sample was placed in the bottom cap of the T-fitting and evacuated *via* a rough pump. The sample was then heated to 40 °C for sublimation, after which the variable leak valve was opened to produce a stable chamber pressure of approximately  $1\text{--}2 \times 10^{-7}$  mbar, although higher pressures ( $4$  or  $7 \times 10^{-7}$  mbar) were used for particularly low-intensity fragments ( $[\text{CpFeMn}(\text{CO})]^-$  and  $[\text{Mn}(\text{CO})_4]^-$ , respectively).

The effusive gaseous precursor beam produced by sublimation enters the interaction zone within the chamber *via* a stainless steel capillary. Within the interaction zone, it crosses an energetically well-defined electron beam generated by a trochoidal electron monochromator (TEM). This electron beam was energetically calibrated to the  $[\text{SF}_6]^-/\text{SF}_6$  ion yield, which peaks in intensity at 0 eV. The energy resolution of the electron beam was estimated from the full width at half maximum (FWHM) of the ion yield produced *via* this resonance and was found to be in the range from 120 to 130 meV during the current experiments. Ionic fragments produced in DEA and DI to  $(\eta^3\text{-Cp})\text{Fe}(\text{CO})_2\text{Mn}(\text{CO})_5$  were measured using a Hiden EPIC1000 quadrupole mass spectrometer (Hiden Analytical, Warrington UK) equipped with two separate RF generators, which operate within a high (2–1000) and low (0.4–50) *m/z*-range. Ion yields for fragments observed through DEA were recorded by setting the quadrupole mass filter to only allow transmission of the selected *m/z* ratio and scanning the electron energy. Positive ion mass spectra were recorded by scanning through the relevant mass range at fixed electron energy. The background pressure of the vacuum chamber was approximately  $1 \times 10^{-8}$  mbar and the TEM was maintained at a constant temperature of 120 °C using halogen lamps in order to prevent deposition of the gaseous precursor onto its lens components.

### 2.3 Quantum chemical calculations

All quantum chemical calculations were carried out using the ORCA program, version 4.0.<sup>42</sup> Geometries of the molecule and the fragments were optimized using the density functional BP86<sup>43,44</sup> and the def2-TZVP basis set<sup>45</sup> including the D3BJ dispersion correction.<sup>46,47</sup> Harmonic vibrational frequencies at the

same level of theory were used to derive zero-point energies and the thermal vibrational and rotational energy of the neutral molecule. Threshold energies were calculated by single-point coupled cluster calculations at the DLPNO-CCSD(T) level of theory<sup>48–51</sup> using basis sets aug-cc-pVTZ and aug-cc-pVQZ.<sup>52,53</sup> Quasi-restricted orbitals<sup>54</sup> (derived from the UHF orbitals) were used to define a reference determinant in the open-shell coupled cluster calculations that reduces spin contamination and were also used in the electronic structure analysis at the DFT level. Localized orbital analysis was performed using the IAO–IBO protocol by Knizia<sup>55</sup> and bond orders were calculated according to Mayer.<sup>56–59</sup>

Threshold calculations at the DLPNO-CCSD(T) level of theory were performed with both diffuse triple zeta and diffuse quadruple zeta basis sets in order to monitor basis set convergence and minimize basis set errors. It should be noted here that we previously found for the potential organometallic FEBID precursor  $(\eta^3\text{-C}_3\text{H}_5)\text{Ru}(\text{CO})_3\text{Br}$ <sup>60</sup> that the use of coupled cluster calculations gave more accurate predictions of the threshold values than the GGA DFT BP86 functional. In that study, an approximate parameterized coupled cluster method, pCCSD/2a, was used in conjunction with the older local pair natural orbital (LPNO) methodology that reduces the dramatic scaling of coupled cluster methods. While the pCCSD/2a approximation is a decent approximation to CCSD(T), with the availability of the more favourable and more accurate domain local pair natural orbital (DLPNO) methodology for open-shell systems and the CCSD(T) method, it is now possible to perform even more accurate DLPNO-CCSD(T) calculations at similar computational cost. However, in the current case, the thresholds at the BP86 and DLPNO-CCSD(T) levels of theory are overall quite similar for this molecule, though they notably differ in one case by 1.1 eV (see Table 1 in the Results and discussion section). As discussed in the previous study of  $(\eta^3\text{-C}_3\text{H}_5)\text{Ru}(\text{CO})_3\text{Br}$ ,<sup>60</sup> we estimate these thresholds to be accurate within  $\pm 0.2$  eV.

## 3 Results and discussion

### 3.1 Dissociative electron attachment to $\text{CpFe}(\text{CO})_2\text{Mn}(\text{CO})_5$ in the gas phase

Negative ion yields produced by DEA to  $\text{CpFe}(\text{CO})_2\text{Mn}(\text{CO})_5$  are shown in Fig. 2 and 3. The yields have been normalized to the

**Table 1** Calculated thresholds (in eV) for electron attachment and dissociation to produce  $[\text{Mn}(\text{CO})_5]^-$ ,  $[\text{CpFeMn}(\text{CO})_6]^-$  (as  $[\text{CpFe}(\text{CO})_2\text{Mn}(\text{CO})_4]^-$  and  $[\text{CpFe}(\text{CO})\text{Mn}(\text{CO})_5]^-$ ), and  $[\text{Mn}(\text{CO})_4]^-$ .  $[\text{Mn}(\text{CO})_5]^-$  is produced by rupture of the Fe–Mn bond, and can be accompanied by the loss of one or two CO ligands from the Fe-centred moiety. Based on the calculated thresholds, it is likely that single CO loss from the Fe-centred fragment contributes in part to the higher-energy tail of the ion yield of  $[\text{Mn}(\text{CO})_5]^-$ ; it is, however, unlikely that double CO loss contributes to this signal. At energies above 0.5 eV, carbonyl loss from the  $[\text{Mn}(\text{CO})_5]^-$  fragment leads to the formation of  $[\text{Mn}(\text{CO})_4]^-$

Anionic fragment		Neutral fragment A	Neutral fragment B	Threshold (BP86, eV)	Threshold (CC, TZ, eV)	Threshold (CC, QZ, eV)	Threshold (exp, eV)
$\text{M}^-$		—	—	–2.4	–2.5	–2.5	—
$\text{Mn}(\text{CO})_5$	(c)	$\text{CpFe}(\text{CO})_2$	—	–1.6	–1.8	–1.8	0.0
$\text{Mn}(\text{CO})_5$	(a1)	$\text{CpFe}(\text{CO})$	CO	1.0	0.5	0.5	—
$\text{Mn}(\text{CO})_5$	(a2)	CpFe	2CO	3.7	2.6	2.5	—
$\text{CpFe}(\text{CO})\text{Mn}(\text{CO})_5$	(a)	CO	—	–0.9	–1.2	–1.3	0.0
$\text{CpFe}(\text{CO})_2\text{Mn}(\text{CO})_4$	(b)	CO	—	–1.4	–1.4	–1.5	—
$\text{Mn}(\text{CO})_4$		$\text{CpFe}(\text{CO})_2$	CO	0.9	0.5	0.5	0.5

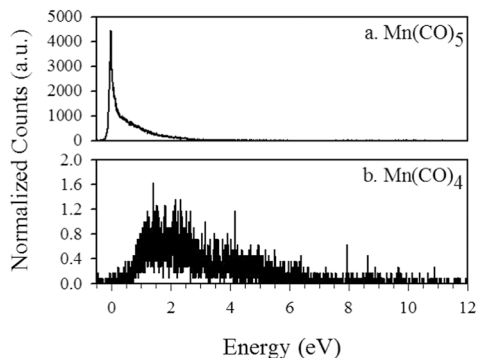


Fig. 2 Negative ion yield spectra of  $[\text{Mn}(\text{CO})_5]^-$  and  $[\text{Mn}(\text{CO})_4]^-$ .  $[\text{Mn}(\text{CO})_5]^-$  is the dominant fragment observed in DEA to  $(\eta^5\text{-Cp})\text{Fe}(\text{CO})_2\text{Mn}(\text{CO})_5$ , followed closely by  $[\text{CpFeMn}(\text{CO})_6]^-$  (see Fig. 3a).  $[\text{Mn}(\text{CO})_5]^-$  is most efficiently produced by direct Fe–Mn bond rupture, although it may be produced *via* a number of pathways (see Fig. 4 and Table 1), a combination of which likely contribute to the high energy tail of the ion yield.

pressure of  $\text{CpFe}(\text{CO})_2\text{Mn}(\text{CO})_5$  present in each experiment and are expressed at a nominal target pressure of  $1 \times 10^{-7}$  mbar of the precursor. In order to aid the interpretation, we have calculated the thresholds for the most relevant DEA pathways using quantum chemistry at the BP86 and DLPNO-CCSD(T) levels of theory. These channels are the loss of one CO and the cleavage of the Fe–Mn bond leading to the formation of  $[\text{Mn}(\text{CO})_5]^-$ . The threshold for the latter is calculated for cases where (i) the neutral  $\text{CpFe}(\text{CO})_2$  fragment stays intact, (ii) the neutral fragment loses one CO ligand or (iii) the neutral fragment loses both ligands. The threshold values calculated at the DLPNO-CCSD(T)/aug-cc-pVQZ level of theory are shown in an energy diagram in Fig. 4, along with the respective optimized molecular structures. The respective threshold values for all fragments calculated are also given in Table 1, along with their experimentally observed appearance energies. For comparison, we have also calculated the thermochemical threshold for the formation of  $[\text{CpFe}(\text{CO})_2]^-$ , although this fragment is not observed.

The stoichiometries of the two most intense fragments produced are  $[\text{Mn}(\text{CO})_5]^-$  and  $[\text{CpFeMn}(\text{CO})_6]^-$ , corresponding to the  $m/z$  ratios 195 and 344, respectively. Both fragments are produced with appreciable intensity *via* a low-lying resonance with maximum contribution to the ion yield near 0 eV. The thermochemical thresholds for these reactions calculated at the DLPNO-CCSD(T)/aug-cc-pVQZ level of theory are  $-1.8$  and  $-1.5$  eV respectively. Correspondingly, the significant contribution through these fragments is as expected, as electron attachment is most efficient close to 0 eV<sup>31</sup> and the survival probability of the TNI is highest at low energies.<sup>30</sup> Further, such efficient low-energy dissociation channels must be exothermic, and this is clearly the case for both these channels as can be seen from Fig. 4 and Table 1.

From the fragments observed, the single carbonyl loss fragment  $[\text{CpFeMn}(\text{CO})_6]^-$  has the highest relative peak intensity, which reaches a maximum at 0.15 eV and then tapers off to

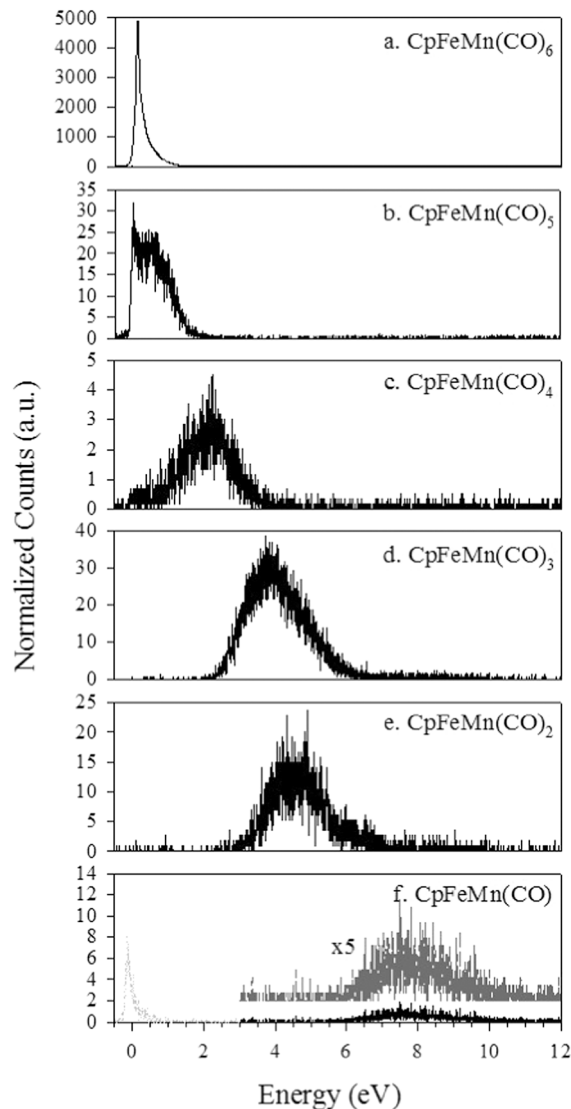
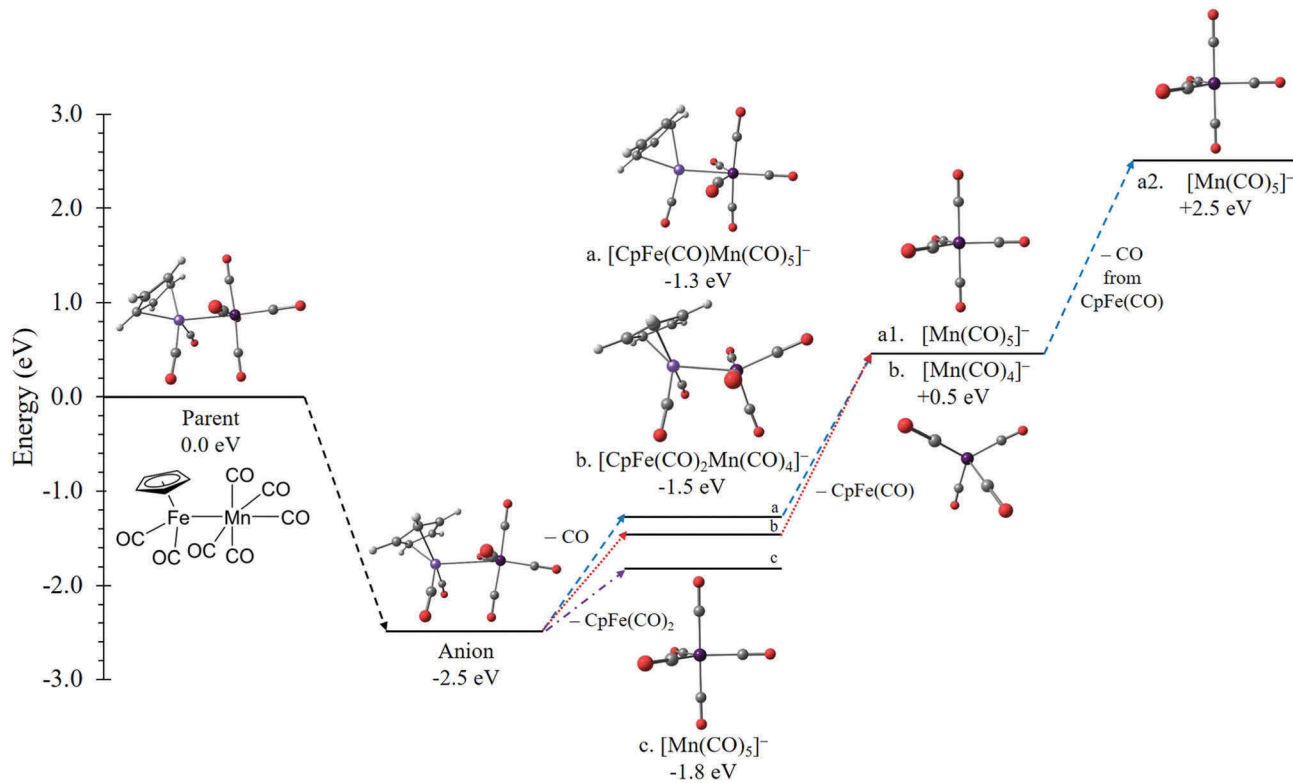


Fig. 3 Negative ion yield spectra of  $[\text{CpFeMn}(\text{CO})_{6-n}]^-$ , where  $n = 0-5$ . Each molecular formula is written stoichiometrically; for example, it is likely that  $[\text{CpFe}(\text{CO})_2\text{Mn}(\text{CO})_4]^-$  and  $[\text{CpFe}(\text{CO})\text{Mn}(\text{CO})_5]^-$  both contribute to the ion yield of  $[\text{CpFeMn}(\text{CO})_6]^-$  (see Table 1).  $[\text{Mn}(\text{CO})_5]^-$  (Fig. 2a) and  $[\text{CpFeMn}(\text{CO})_6]^-$  show signs of being competing pathways (see Fig. 4).

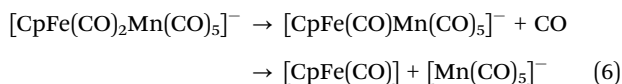
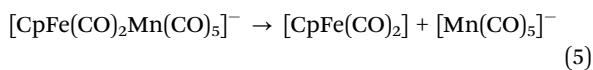
the baseline at about 2 eV. However, the  $[\text{Mn}(\text{CO})_5]^-$  fragment produced by the rupture of the Fe–Mn bond has the highest integrated relative DEA cross-section. Notably, the  $[\text{Mn}(\text{CO})_5]^-$  intensity peaks at 0 eV – lower than  $[\text{CpFeMn}(\text{CO})_6]^-$  – and decreases as the single CO loss fragment intensity increases. At approximately 0.15 eV, where the single CO loss has peaked, the  $[\text{Mn}(\text{CO})_5]^-$  peak broadens, maintaining appreciable intensity up to about 4 eV.

The energy dependencies of these two fragments thus bear signs of competing channels, which is typical for metastable decay processes. Although  $[\text{CpFeMn}(\text{CO})_6]^-$  can only be produced *via* single carbonyl loss, formation of  $[\text{Mn}(\text{CO})_5]^-$  may be produced directly (eqn (5) and path c in Fig. 4), or it may be preceded by an initial CO ligand loss from the  $\text{CpFe}(\text{CO})_2$



**Fig. 4** A visualization of calculated thresholds of electron attachment and dissociation to produce  $[\text{Mn}(\text{CO})_5]^-$ ,  $[\text{CpFeMn}(\text{CO})_6]^-$  (as  $[\text{CpFe}(\text{CO})_2\text{Mn}(\text{CO})_4]^-$  and  $[\text{CpFe}(\text{CO})\text{Mn}(\text{CO})_5]^-$ ), and  $[\text{Mn}(\text{CO})_4]^-$ . Electron attachment to the neutral parent molecule is exothermic by 2.5 eV and produces the parent anion. The Fe–Mn bond in the parent anion may then rupture (path c), producing  $[\text{Mn}(\text{CO})_5]^-$ ; this overall reaction is exothermic by 1.8 eV. Alternatively, the parent anion can lose a carbonyl ligand, either from the Fe-centred moiety (path a, producing  $[\text{CpFe}(\text{CO})\text{Mn}(\text{CO})_5]^-$ , exothermic by 1.3 eV) or from the Mn-centred moiety (path b, producing  $[\text{CpFe}(\text{CO})_2\text{Mn}(\text{CO})_4]^-$ , exothermic by 1.5 eV). Both paths are expected to contribute to the ion yield at the current experimental temperature. The Fe–Mn bond in either of these product anions may then rupture, producing  $[\text{Mn}(\text{CO})_5]^-$  (via path a1, from  $[\text{CpFe}(\text{CO})\text{Mn}(\text{CO})_5]^-$ ) or  $[\text{Mn}(\text{CO})_4]^-$  (via path b1, from  $[\text{CpFe}(\text{CO})_2\text{Mn}(\text{CO})_4]^-$ ). Both overall reactions are endothermic by 0.5 eV. Finally, a second CO can be lost from the neutral CpFe(CO) fragment produced by Fe–Mn bond rupture via path a2, producing  $[\text{Mn}(\text{CO})_5]^-$ . This reaction, however, is endothermic by 2.5 eV and is not expected to contribute significantly to the  $[\text{Mn}(\text{CO})_5]^-$  ion yield.

moiety before the Fe–Mn bond rupture takes place (eqn (6) and path a in Fig. 4):



The direct formation of  $[\text{Mn}(\text{CO})_5]^-$  and  $[\text{CpFe}(\text{CO})\text{Mn}(\text{CO})_5]^-$ , as stated above, was calculated to be exothermic by 1.8 eV and 1.3 eV, respectively. The threshold for Fe–Mn bond dissociation accompanied by a single CO loss from the Fe centre, conversely, was found to be endothermic by 0.5 eV (see Table 1 and path a1 in Fig. 4). Given the broadening of the ion yield of  $[\text{Mn}(\text{CO})_5]^-$  above approximately 0.2 eV, it is likely that both these reactions contribute to the negative ion yield spectrum. While the direct dissociation is predominant below 0.2 eV, the contribution through preceding CO loss from the iron moiety (eqn (6) and path a1 in Fig. 4) is likely to be significant above that energy. The Fe–Mn bond dissociation accompanied by two CO ligands dissociating from the Fe centre (path a2 in Fig. 4) was found to

be endothermic by 2.5 eV and could thus in principle contribute to the  $[\text{Mn}(\text{CO})_5]^-$  ion yield above this energy, though this would clearly be a minor (if extant) contribution.

In this context, it should be noted that our observation window is the first 10  $\mu\text{s}$  after electron attachment. This is the extraction time from the ionization region. Ions that fragment further during the flight through the quadrupole mass filter, which takes about 50  $\mu\text{s}$ , do not maintain stable trajectories and are therefore not detected. Further, considering the energy resolution of the electron beam and the internal energy distribution of the parent molecule at the current experimental temperature ( $T = 40^\circ\text{C}$ ), the appearance energy may be shifted below the actual thermochemical threshold.

Independent of the route of formation for  $[\text{Mn}(\text{CO})_5]^-$  at higher energies (above about 0.2 eV), the formation of  $[\text{CpFeMn}(\text{CO})_6]^-$  may in principle proceed through the loss of CO from the iron containing moiety, producing  $[\text{CpFe}(\text{CO})\text{Mn}(\text{CO})_5]^-$ , or from the manganese containing moiety, producing  $[\text{CpFe}(\text{CO})_2\text{Mn}(\text{CO})_4]^-$  (routes a and b in Fig. 4, respectively). These fragments are not distinguishable by means of mass spectrometry, so calculations were performed to deduce which isomer is more likely to dominate under the current experimental

conditions. At the DLPNO-CCSD(T) level of theory using the aug-cc-pVQZ basis set, we find the threshold for the formation of  $[\text{CpFe}(\text{CO})\text{Mn}(\text{CO})_5]^-$  to be  $-1.3$  eV and that for  $[\text{CpFe}(\text{CO})_2\text{Mn}(\text{CO})_4]^-$  to be  $-1.5$  eV. It is thus not obvious that the formation of one isomer rather than the other dominates at 0 eV. However, though with low intensity, we observe the formation of  $[\text{Mn}(\text{CO})_4]^-$  with an appearance energy of about 0.5 eV, which is in good agreement with the calculated threshold of 0.5 eV (see Table 1). In principle,  $[\text{Mn}(\text{CO})_4]^-$  formation may proceed *via* CO loss from the  $[\text{Mn}(\text{CO})_5]^-$  fragment or *via* dissociation of the Fe–Mn bond in the  $[\text{CpFe}(\text{CO})_2\text{Mn}(\text{CO})_4]^-$  fragment and the threshold is indifferent to which of these paths lead to the formation of this fragment. However, the very low intensity of  $[\text{Mn}(\text{CO})_4]^-$ ,  $<0.5\%$  of that for the formation of  $[\text{Mn}(\text{CO})_5]^-$  at the same energy (around 1.5 eV), indicates insignificant CO loss from the Mn containing moiety of the initially formed TNI. We therefore expect the single CO loss from the iron moiety (path a in Fig. 4) to be the dominant initial CO loss channel rather than loss from the  $\text{Mn}(\text{CO})_5$  unit (path b in Fig. 4).

In addition to the major fragments and the formation of  $[\text{Mn}(\text{CO})_4]^-$  (Fig. 2b), we observe further CO loss from  $[\text{CpFeMn}(\text{CO})_6]^-$ , leading to the fragments  $[\text{CpFeMn}(\text{CO})_{6-n}]^-$  with  $n = 1-5$  (Fig. 3b–f). No cyclopentadienyl loss is observed, unlike in some similar organometallic species.<sup>20,61</sup> As mentioned above, the formation of  $[\text{Mn}(\text{CO})_4]^-$  is a minor channel and, at their respective maxima, its intensity is more than 3 orders of magnitude less than that of  $[\text{Mn}(\text{CO})_5]^-$ .

The formation of the fragments  $[\text{CpFeMn}(\text{CO})_{6-n}]^-$  with  $n = 1$  and 2 is attributed to further CO loss from  $[\text{CpFeMn}(\text{CO})_6]^-$  through the same low energy resonance(s) that led to the formation of  $[\text{CpFeMn}(\text{CO})_6]^-$ ,  $[\text{Mn}(\text{CO})_5]^-$  and  $[\text{Mn}(\text{CO})_4]^-$ . Here, hot band transitions from the high energy tail of the Maxwell-Boltzmann distribution of internal energies at the current experimental temperature are likely to constitute the main contribution to the sharp 0 eV feature in the  $[\text{CpFeMn}(\text{CO})_5]^-$  yield. The fragments  $[\text{CpFeMn}(\text{CO})_{6-n}]^-$  with  $n = 3$  and 4, conversely, appear exclusively through fairly broad, but distinct contributions peaking close to 3.8 and 4.5 eV, respectively. We attribute these contributions to a distinct, higher-lying resonance associated with one of the first HOMO–LUMO transitions in this molecule, *i.e.* a core-excited resonance. The shift of the  $[\text{CpFeMn}(\text{CO})_2]^-$  ion yield towards higher energy with respect to that of  $[\text{CpFeMn}(\text{CO})_3]^-$  is accordingly attributed to the higher threshold for the formation of this fragment, making this channel more competitive through the higher energy side of the resonance. We note, however, that we cannot exclude contributions from higher-lying shape resonances at these energies. Finally, the loss of all but one CO, forming  $[\text{CpFeMn}(\text{CO})]^-$ , proceeds explicitly through a yet higher-lying resonance, appearing through a contribution to the ion yield in the region from 6–10 eV with a maximum at about 8 eV.

As discussed above, metal–metal bond cleavage leading to the formation of  $[\text{Mn}(\text{CO})_5]^-$  is one of the two dominant channels observed in DEA to  $[\text{CpFe}(\text{CO})_2\text{Mn}(\text{CO})_5]$ ; the counter fragment  $[\text{CpFe}(\text{CO})_2]^-$  with charge retention on the iron-centred moiety is not observed. The strongly electron-donating Cp anion ligand on

the Fe centre, when compared to the 5  $\pi$ -acid CO ligands on the Mn centre, produces an electron-rich iron centred moiety in the neutral parent molecule. The calculated electron affinity of  $[\text{CpFe}(\text{CO})_2]$  is positive (1.64 eV, although the electron affinity of  $[\text{Mn}(\text{CO})_5]$  is about 0.9 eV greater) and the formation of  $[\text{CpFe}(\text{CO})_2]^-$  from  $[\text{CpFe}(\text{CO})_2\text{Mn}(\text{CO})_5]$  is exothermic by about 0.42 eV. It is therefore thermochemically possible for the charge to be retained by the iron-centred moiety after Fe–Mn bond cleavage; however, this is not observed. This observation is readily explained by the charge distribution within the initially formed TNI and its evolution during the separation of the metal-centred fragments: *i.e.* its dissociation dynamics.

To get a better understanding of the cleavage of the metal dimer in the attachment process and formation of  $[\text{Mn}(\text{CO})_5]^-$  it is useful to first consider the neutral molecule. For this purpose Fig. 5 shows several relevant molecular orbital isosurfaces of both the neutral precursor and the ground state anion. The metal–metal bonding orbital of the neutral precursor is shown in Fig. 5a (HOMO–2), while the lowest unoccupied orbital of the neutral precursor (LUMO) is shown in Fig. 5b. The spin density distribution within the ground state anion and the singly occupied HOMO of the relaxed molecular anion (SOMO) are shown in Fig. 5c and d, respectively. All isosurfaces shown are computed at the BP86 level of theory. Finally, Fig. 6 shows the results of an orbital analysis of the dissociating molecular anion, depicting a relaxed surface scan of the anion where the Mn–Fe distance was varied from 2.81 Å to 4.84 Å.

According to X-ray crystallography the Mn–Fe distance is 2.843 Å,<sup>40</sup> while our gas phase DFT calculations give a bond length of 2.81 Å, indicative of a single metal–metal bond similar to the 2.89 Å Mn–Mn bond length of  $\text{Mn}_2(\text{CO})_{10}$ . Analysis of the occupied canonical molecular orbitals reveal that the HOMO–2 (Fig. 5a) can be described as essentially a d-based  $\sigma$ -bonding orbital between Fe and Mn. A localized orbital analysis confirms that a stable 2-electron  $\sigma$ -bond exists, and a Mayer bond order of 0.4 between Mn and Fe is calculated (this can be

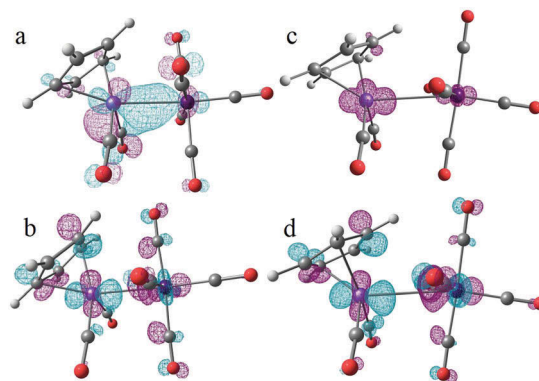
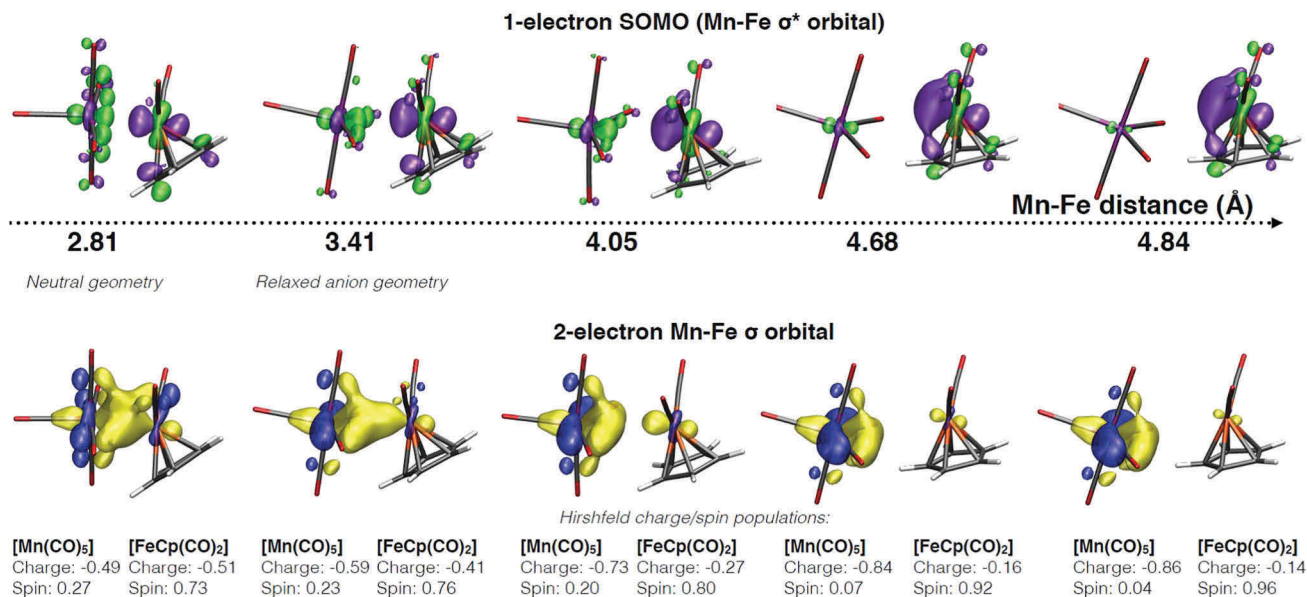


Fig. 5 Calculated orbital isosurfaces of: (a) the Mn–Fe  $\sigma$ -bonding orbital (HOMO–2) of the neutral  $(\eta^5\text{-Cp})\text{Fe}(\text{CO})_2\text{Mn}(\text{CO})_5$  molecule, (b) the LUMO of the neutral  $(\eta^5\text{-Cp})\text{Fe}(\text{CO})_2\text{Mn}(\text{CO})_5$  molecule, (c) the spin density map of the  $[(\eta^5\text{-Cp})\text{Fe}(\text{CO})_2\text{Mn}(\text{CO})_5]^-$  anion and (d) the SOMO of the  $[(\eta^5\text{-Cp})\text{Fe}(\text{CO})_2\text{Mn}(\text{CO})_5]^-$  anion. Interestingly, the electron attaches into an orbital largely located on the Fe atom, while the charge upon separation of the two metal-centred moieties is retained by the Mn-centred fragment.



**Fig. 6** Elongation of the Mn–Fe bond upon electron attachment. The top part of this figure shows the changing geometry of the singly occupied Mn–Fe  $\sigma^*$  antibonding orbital as the distance between the two metal centres increases, while the bottom part shows the changing geometry of the doubly occupied Mn–Fe  $\sigma$ -bonding orbital (IAO–IBO localized orbital), as well as the Hirshfeld charges and spin populations of the two metal-centred moieties. The electron of the singly occupied  $\sigma^*$  orbital remains primarily on the Fe-centred moiety, producing the spin density map seen in Fig. 5c. The electrons of the doubly occupied  $\sigma$  orbital, however, remain primarily on the Mn-centred moiety, resulting in the experimentally-observed negative charge on the Mn-centred fragments  $[\text{Mn}(\text{CO})_5]^-$  and  $[\text{Mn}(\text{CO})_4]^-$ .

compared to a Mayer bond order of 0.94–1.17 for the Mn–C bonds). The LUMO of the neutral parent molecule (Fig. 5b) is revealed to be the  $\sigma^*$  antibonding counterpart of the Mn–Fe bonding orbital.

Analysis of the SOMO of the parent anion (Fig. 5d), reveals that it is quite similar to the LUMO, suggesting that electron attachment can be envisioned as the attached electron occupying the LUMO of the neutral. As the LUMO is an antibonding Mn–Fe  $\sigma^*$  orbital, occupation of this orbital should lead to elongation of the Mn–Fe bond; in fact, the Mn–Fe bond elongates from 2.81 Å in the neutral to 3.41 Å in the relaxed geometry of the anion. While this analysis corresponds well with the major dissociation channel involving Fe–Mn bond rupture, the SOMO of the anion as well as the spin density (Fig. 5c) reveal that the attached electron is actually more on the Fe-based fragment than the Mn. The dynamics behind the charge retention in this dissociation process can be readily understood by analysis of a relaxed surface scan of the initially formed anion, as shown in Fig. 6. Here, the Fe–Mn bond length was systematically increased from the parent molecule bond length of 2.81 Å to 4.84 Å, producing the experimentally observed  $\text{FeCp}(\text{CO})_2$  and  $[\text{Mn}(\text{CO})_5]^-$  fragments. The 1-electron SOMO orbital gradually changes from a slightly Fe-centric Mn–Fe  $\sigma^*$  orbital in the 2.81 Å structure to a more localized Fe d-orbital in the 4.84 Å structure. This confirms that the attached electron is retained by the neutral  $\text{FeCp}(\text{CO})_2$  fragment. The 2-electron Mn–Fe  $\sigma$ -bonding orbital, however, gradually changes as well (here shown as a localized orbital from IAO–IBO analysis), and ultimately resides on the Mn-centred moiety. As the 2 electrons in the Mn–Fe bonding orbital are therefore retained by the Mn, this produces a  $[\text{Mn}(\text{CO})_5]^-$  anionic

fragment. A Hirshfeld population analysis (also shown in Fig. 6) of the electron distribution within the anion demonstrates this picture as well, with the anionic charge residing on the closed-shell  $[\text{Mn}(\text{CO})_5]^-$  fragment with a Mn(1–) oxidation state,  $d^8$  (due to Mn retaining the 2 electrons of the Mn–Fe bond), and the spin residing on the open-shell Fe fragment with a Fe(1+) oxidation state. This reveals the final picture of the dissociation dynamics wherein the attached electron ends upon a different fragment (Fe) than the negative charge (Mn).

### 3.2 Dissociative ionization of $\text{CpFe}(\text{CO})_2\text{Mn}(\text{CO})_5$ in the gas phase

Dissociative ionization spectra of  $\text{CpFe}(\text{CO})_2\text{Mn}(\text{CO})_5$  recorded at 70 eV impact energy are shown in Fig. 7. Dissociative ionization is a non-resonant process that sets in at or above the ionization threshold of the parent molecule and increases in efficiency with increasing incident electron energy before levelling off between 50 and 100 eV. Close to the ionization threshold, single bond ruptures commonly dominate the DI spectra; as the energy increases, contributions from more extensive fragmentation reactions increases. The spectra shown in Fig. 7 are recorded at 70 eV, which is close to the maxima of all channels and thus gives a good picture of the relative integral cross sections for individual channels in the SE energy range relevant in FEBID. For completeness, Table S1 (ESI<sup>†</sup>) compares the relative intensities for the individual fragments recorded at 30, 40, 50 and 60 eV, showing that no significant changes are in this energy range.

The most intense fragment produced by dissociative ionization of  $\text{CpFe}(\text{CO})_2\text{Mn}(\text{CO})_5$  at 70 eV is  $[\text{CpFe}]^+$ , followed by

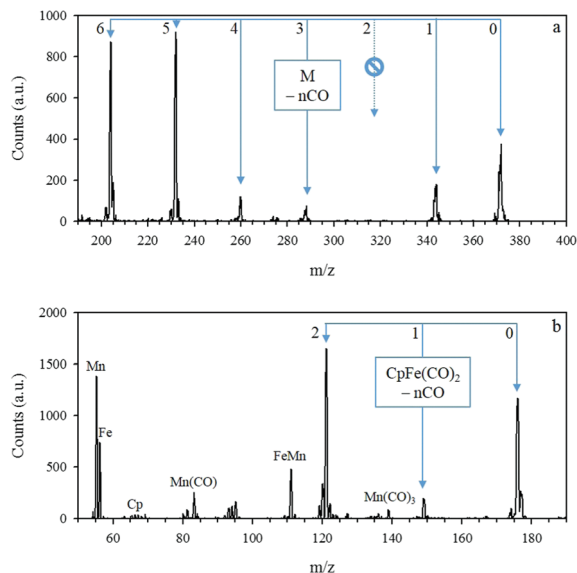


Fig. 7 DI spectra of  $(\eta^5\text{-Cp})\text{Fe}(\text{CO})_2\text{Mn}(\text{CO})_5$  with an incident electron energy of 70 eV. (a) Shows the  $\text{M} - n\text{CO}$  ( $n = 0-6$ ) progression, which interestingly excludes  $n = 2$ , likely due to fast decay processes. (b) Shows the  $\text{CpFe}(\text{CO})_2 - n\text{CO}$  ( $n = 0-2$ ) progression, which exhibits some similar behaviour as well as the naked metal fragments,  $\text{Mn}(\text{CO})$  and the low intensity contribution from the cyclopentadienyl ring. The low intensity features at  $m/z = 275$  and  $95$  are attributed to contaminants within the vacuum chamber.

$[\text{CpFe}(\text{CO})_2]^+$ ,  $[\text{CpFeMn}(\text{CO})_2]^+$  and  $[\text{CpFeMn}(\text{CO})]^+$ . There is thus significantly more extensive fragmentation observed through DI of  $\text{CpFe}(\text{CO})_2\text{Mn}(\text{CO})_5$  than through DEA. Similar to DEA, however, the DI spectra is characterized through two principal processes: (a) progressive CO loss from the Fe–Mn moiety and (b) cleavage of the Fe–Mn bond to produce  $[\text{CpFe}(\text{CO})_2]^+$ , followed by additional CO loss. Fig. 7a shows a DI mass spectrum for  $\text{CpFe}(\text{CO})_2\text{Mn}(\text{CO})_5$  in the  $m/z$  range from 190 to 400, which encompasses the CO ligand loss progression. As in DEA, 1–6 CO ligands are lost within this progression; however, DI favours much more complete fragmentation, with  $[\text{M} - 5\text{CO}]^+$  and  $[\text{M} - 6\text{CO}]^+$  ( $[\text{CpFeMn}(\text{CO})_2]^+$  and  $[\text{CpFeMn}(\text{CO})]^+$ ) being the most abundant fragments. Interestingly,  $[\text{M} - 2\text{CO}]^+$  ( $[\text{CpFeMn}(\text{CO})_5]^+$ ) is simply missing from the spectra and  $[\text{M} - 3\text{CO}]^+$  ( $[\text{CpFeMn}(\text{CO})_4]^+$ ) and  $[\text{M} - 4\text{CO}]^+$  ( $[\text{CpFeMn}(\text{CO})_3]^+$ ) only appear with low intensity. We attribute this to the relative stabilities of intermediates associated with the formation of these fragments. In order to determine this, we examined the energetic thresholds for the formation of several fragments relevant to this process. The adiabatic ionisation energy of  $\text{CpFeMn}(\text{CO})_7$  was calculated at the DLPNO-CCSD(T) level of theory using the aug-cc-pVTZ basis set, and was found to be 6.4 eV. Thresholds for the formation of  $[\text{CpFeMn}(\text{CO})_6]^+$  and  $[\text{CpFeMn}(\text{CO})_5]^+$  at the same level of theory were found to be 7.4 and 9.3 eV, respectively. However, the ground state of the  $[\text{CpFeMn}(\text{CO})_5]^+$  fragment was found to have three bridging CO, similar to the structure previously calculated for the ground state of the neutral  $\text{CpFeMn}(\text{CO})_5$ .<sup>62</sup> The ground state of the  $[\text{CpFeMn}(\text{CO})_6]^+$  fragment, on the other hand, was found to have one bridging carbonyl.

These structures are shown along with the respective threshold values in Fig. S1 and Table S2 with the ESI.† We anticipate that the rearrangement and internal energy redistribution within  $[\text{CpFeMn}(\text{CO})_5]^+$  is slow compared to further CO loss: *i.e.* the subsequent CO loss producing  $[\text{CpFeMn}(\text{CO})_4]^+$ , *etc.*, takes place before rearrangement to the triply-bridged ground state and the consequent stabilization of the fragment with respect to further CO loss is complete. This in turn reduces its lifetime to such an extent that it is not detected within the current observation time window (see above). A similar situation must apply for  $[\text{CpFeMn}(\text{CO})_4]^+$  and  $[\text{CpFeMn}(\text{CO})_3]^+$ ; however, as these have dispersed energy by the dissociation of 3 and 4 CO units, respectively, a fraction of these ions still survives the approximately 50  $\mu\text{s}$  flight through the quadrupole mass filter. Hence, while long-lived metastable intermediates may persist long enough to be detected by the mass spectrometer, short-lived intermediates will not. We thus conclude that  $[\text{CpFeMn}(\text{CO})_5]^+$  must quickly decay through further CO loss, while  $[\text{CpFeMn}(\text{CO})_7]^+$  and  $[\text{CpFeMn}(\text{CO})_6]^+$  are metastable products with longer decay times. Finally, the fragments  $[\text{CpFeMn}(\text{CO})_2]^+$  and  $[\text{CpFeMn}(\text{CO})]^+$  are expected to have discharged the bulk of the initial internal energy through the extensive CO loss leading to their formation and thus have comparably long lifetimes.

Fragment formation in the  $m/z$  range from 50 to 90 is shown in Fig. 7b. The major contribution in this  $m/z$  range is through cleavage of the Fe–Mn bond to produce  $[\text{CpFe}(\text{CO})_2]^+$ , accompanied by further CO loss. Here we see similar behaviour to that observed for sequential CO loss from the molecular cation: although  $[\text{CpFe}(\text{CO})_2]^+$  and  $[\text{CpFe}]^+$  are abundant products,  $[\text{CpFe}(\text{CO})]^+$  is only observed with marginal intensity. We attribute this to  $[\text{CpFe}(\text{CO})]^+$  similarly being an unstable decay intermediate that generally fragments further, too quickly to be observed in the current experiment. The bare  $[\text{FeMn}]^+$  cation, as well as both the bare  $\text{Fe}^+$  and  $\text{Mn}^+$  cations, are also observed with appreciable intensity *via* DI. The cyclopentadienyl ligand, on the other hand, is only observed with low intensity, and no significant fragmentation of the cyclopentadienyl is observed. This is unlike previous observations in DI of  $\text{MeCpPtMe}_3$ ,<sup>20</sup> where hydrogen loss and fragmentation of the MeCp ligand dominates the DI spectra, an effect that may be explained by the changed ion stabilities of H-loss products in the alkylated Cp derivative.

### 3.3 Dissociative electron attachment vs. dissociative ionization and comparison of gas phase and surface experiments

Table 2 compares the relative intensities of all DI fragments at 70 eV with the relative intensities of all DEA fragments in the energy range from 0–12 eV. For DI, the relative intensities were calculated by integrating the isotope distribution for each fragment and normalizing it to the single carbonyl loss fragment. For DEA, these were calculated by integrating the intensity of the respective fragments over the energy range from 0–12 eV. In DEA, the two major fragments  $[\text{Mn}(\text{CO})_5]^-$  and  $[\text{CpFeMn}(\text{CO})_6]^-$  are fully dominant: they make up 96% of the total negative ion yield and the remaining fragments are insignificant in comparison.

**Table 2** Comparison of relative intensities of all DI fragments at 70 eV with those of all DEA fragments in the energy range from 0–12 eV. Relative DI intensities were calculated by integrating the isotope distribution for each fragment and normalizing to the single carbonyl loss fragment. For DEA these were calculated by integrating the intensity of the respective fragments over the energy range from 0–12 eV and normalizing again to the single carbonyl loss fragment. All relative intensities were pressure normalized. Average CO loss per incident was calculated by multiplying the relative intensity of each fragment by number of carbonyls lost and dividing by the total intensity of all fragments. The upper limit of CO loss was calculated by assuming total CO loss from any neutral counterparts, while the lower bound was calculated by assuming no neutral species fragmentation

Mass	Fragment	DEA	DI
372	CpFeMn(CO) <sub>7</sub>		190
344	CpFeMn(CO) <sub>6</sub>	100	100
316	CpFeMn(CO) <sub>5</sub>	2	
288	CpFeMn(CO) <sub>4</sub>	0.4	31
260	CpFeMn(CO) <sub>3</sub>	5	53
232	CpFeMn(CO) <sub>2</sub>	2	387
204	CpFeMn(CO)	0.3	380
195	Mn(CO) <sub>5</sub>	135	5
177	CpFe(CO) <sub>2</sub>		458
167	Mn(CO) <sub>4</sub>	0.2	7
149	CpFe(CO)		70
139	Mn(CO) <sub>3</sub>		17
121	CpFe		491
111	FeMn/Mn(CO) <sub>2</sub>		4118
83	Mn(CO)		45
66	Cp		15
56	Fe		114
55	Mn		196
44	CO <sub>2</sub>		14
28	CO		185
16	O		6
<hr/>			
Average CO loss	(lower bound)	0.6	3
Average CO loss	(upper bound)	2	6

The fragmentation is much more extensive in DI, where about half of the total fragment intensity comes from CO loss from the molecular ion, with dominant contributions from the loss of 5 and 6 CO. The other half of the intensity is from fragments produced *via* rupture of the Fe–Mn bond, where the main fragments produced are [CpFe(CO)<sub>2</sub>]<sup>+</sup> and [CpFe]<sup>+</sup>, as well as the naked metal cations. For further comparison, we calculated the average CO loss per dissociation incident through DEA and DI by adding up the relative intensities of each fragment multiplied by the number of carbonyl ligands lost and dividing by the total intensity summed over all fragments formed. For fragments associated with Fe–Mn bond rupture, an upper limit of CO loss was calculated by assuming total CO loss from the neutral counterpart, and a lower bound was calculated by assuming no fragmentation of the neutral species. In this way we derive a lower bound of 3 CO ligands lost per DI incident while the upper bound is about 6 CO. The average CO loss per molecule in DEA, conversely, is about 0.6 ligands per molecule if no further CO loss from the neutral counterpart is assumed. The bulk of the negative ion intensity from DEA to CpFe(CO)<sub>2</sub>Mn(CO)<sub>5</sub> is close to 0 eV, below the thermochemical threshold for further CO dissociation from the respective neutral counterparts. Considering the high energy tail of the 0 eV contributions

and the fragments formed at higher energies, it is reasonable to bracket the average CO loss through DEA between 0.6 and 1.0 ligands per event. This demonstrates that significantly more fragmentation of the parent molecule is initiated by DI than by DEA, and deposition of CpFe(CO)<sub>2</sub>Mn(CO)<sub>5</sub> *via* DI in FEBID experiments should produce less carbonaceous deposits than if deposition were to proceed *via* DEA.

To provide a comparison with data from gas phase studies, electron-induced dissociation of CpFe(CO)<sub>2</sub>Mn(CO)<sub>5</sub> molecules adsorbed onto a surface are also presented. Thus, Fig. 8 shows X-ray photoelectron spectroscopy (XPS) data on the changes in the C(1s) and O(2p) regions for 1–2 monolayer films of CpFe(CO)<sub>2</sub>Mn(CO)<sub>5</sub>, adsorbed on a gold surface at about 105 K, and exposed to incremental doses of 500 eV electrons generated from a flood gun source. The precursor was shown to adsorb stoichiometrically at this temperature using XPS. The XPS data in Fig. 8 is part of a larger study conducted at the Johns Hopkins University, designed to provide a comprehensive assessment of various electron and thermal reactions relevant to FEBID.<sup>63</sup> Full details of the experimental setup may be found in Spencer *et al.*<sup>64</sup>

Upon adsorption and prior to electron irradiation, Fig. 8 shows that the C(1s) region contains two major peaks of roughly equal intensity: a lower energy peak at approximately 285.2 eV assigned to the cyclopentadienyl (Cp) carbon atoms, and a higher energy peak at approximately 287.6 eV assigned to the

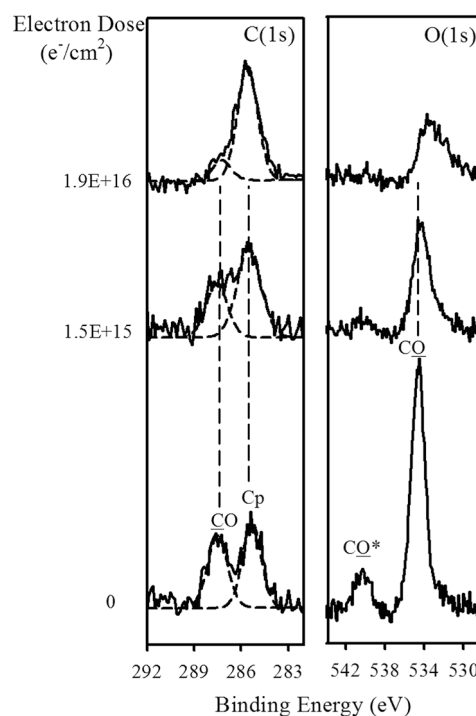


**Fig. 8** XPS analysis of the C(1s) and O(1s) regions for ~0.5–3.0 nm thick films of CpFe(CO)<sub>2</sub>Mn(CO)<sub>5</sub> molecules deposited onto a polycrystalline gold surface at 105 K and exposed to 500 eV electrons. We estimate the thickness of a single monolayer of CpFe(CO)<sub>2</sub>Mn(CO)<sub>5</sub> to be approximately 1.4 nm. The bottom spectra are recorded before electron irradiation (0 electron dose) while the upper traces are recorded after CpFe(CO)<sub>2</sub>Mn(CO)<sub>5</sub> films were exposed to electron doses of  $1.5 \times 10^{15}$  and  $1.9 \times 10^{16}$  e<sup>-</sup> cm<sup>-2</sup>.

carbonyl carbon atoms.<sup>65,66</sup> There is an additional  $\pi$  to  $\pi^*$  shake-up peak (at higher binding energy) associated with the carbonyl (CO) peak; however, it is very weak in intensity and thus cannot be discerned from the background. As the film is exposed to increasing electron doses ( $1.5 \times 10^{15} \text{ e}^- \text{ cm}^{-2}$  and  $1.9 \times 10^{16} \text{ e}^- \text{ cm}^{-2}$ ) there is little change in the Cp peak, but the CO peak intensity decreases significantly in intensity, such that after an electron dose of  $1.9 \times 10^{16} \text{ e}^- \text{ cm}^{-2}$  it is only observed as a small shoulder in the C(1s) spectral envelope. The slight increase in the intensity of the peak assigned to the Cp carbon is attributed to decomposition of remaining CO ligands to graphitic carbon, which has a similar binding energy. Further details can be found in Unlu *et al.*<sup>63</sup> In the O(1s) region, two peaks are initially observed: a narrow peak at 534.5 eV comprising the carbonyl oxygen (CO) and a higher energy  $\pi$  to  $\pi^*$  shake-up peak (CO\*) at 541.2 eV.<sup>65,66</sup> As the electron dose increases the intensity of the main O(1s) peak decreases significantly in intensity, broadens and shifts to a slightly lower binding energy, while the shake-up peak disappears. Changes in the C(1s) and O(1s) regions shown in Fig. 8 are thus consistent with CO desorption from the film occurring as a result of electron irradiation, with no desorption of any carbon atoms from the Cp ring.

Quantitative analysis of the C(1s) and O(1s) areas measured as a function of electron dose, and conducted as part of the study at Johns Hopkins University, revealed that there was no further changes for electron doses in excess of  $1.9 \times 10^{16} \text{ e}^- \text{ cm}^{-2}$ . The oxygen-to-carbon ratio changed from being slightly above the stoichiometric 7:12 O:C ratio (about 0.6:1) prior to electron irradiation to an approximate ratio of 2:7 (about 0.3:1), while the O(1s) area decreases by approximately 70% of its initial value. Based on the stoichiometry of the  $\text{CpFe}(\text{CO})_2\text{Mn}(\text{CO})_5$  molecule, these changes in the O:C ratio and O(1s) area indicate that  $\sim 5$  CO molecules desorb from the surface as the molecularly adsorbed precursor undergoes electron stimulated decomposition. However, in contrast to gas phase experiments, adsorbed precursor molecules are simultaneously exposed to all of the secondary electrons generated by the interaction of the primary beam with the substrate. Consequently, the XPS data shown in Fig. 8 represents the ensemble averaged change in chemical composition in the  $\text{CpFe}(\text{CO})_2\text{Mn}(\text{CO})_5$  film caused by the reactions of these secondary electrons with the adsorbed precursor molecules.

When compared with the gas phase data, however, surface data may allow us to elucidate the likely initial step in the decomposition/deposition of  $\text{CpFe}(\text{CO})_2\text{Mn}(\text{CO})_5$  upon electron impact. In this respect the persistence of the cyclopentadienyl ligand and the loss of CO ligands in the surface experiments is consistent with gas phase observations for both DEA and DI of  $\text{CpFe}(\text{CO})_2\text{Mn}(\text{CO})_5$ . The average number of CO groups lost from the surface in Fig. 8 ( $\sim 5$  CO), is much higher than observed in DEA (0.6–1 CO), but within range of our expectations from DI (3–6 CO). This analysis suggests that the initial step in the electron-induced decomposition of  $\text{CpFe}(\text{CO})_2\text{Mn}(\text{CO})_5$  adsorbed on a surface is driven by DI rather than DEA.

We note, however, that direct comparison between the gas phase and surface data may be called into question, most obviously due to the lack of experimental data on ND, limiting this comparison to

DEA and DI. Further electron-induced or thermally-driven decomposition of intermediates, as well as dissociation through surface activation, may also play a role. Several gas phase and surface studies have been conducted on potential and current FEBID precursors, and electron-induced dissociation is generally found to proceed in two steps (see *e.g.* Thorman *et al.*<sup>11</sup> and references therein, and several more recent surface studies<sup>38,39,63,64,67</sup>). The first of these steps leads to desorption of intact ligands – for  $(\eta^5\text{-Cp})\text{Fe}(\text{CO})_2\text{Mn}(\text{CO})_5$ , this initial step can be identified experimentally by CO desorption, which is detected both by mass spectrometry and by the reduction of the corresponding C(1s) and O(1s) XPS peaks. Further irradiation typically leads to ligand decomposition rather than desorption. This second step can be identified by corresponding changes in the surface observed by XPS, while no ligand desorption is observed by mass spectrometry. The first and second steps may overlap, depending on their respective reaction rates.

For the first process, which is initiated by electron-stimulated precursor decomposition, we believe that parallels may be drawn between the gas phase and surface experiments. The surface studies are generally conducted on inert substrates at low temperatures (typically below  $-120 \text{ }^\circ\text{C}$ ) in order to minimize the potential for any thermal reactions. Finally, effective energy dissipation at surfaces may quench certain dissociation channels,<sup>68</sup> but such effects would in all cases reduce ligand loss and are likely to primarily affect metastable channels rather than direct dissociation channels.

## 4 Conclusions

We have presented gas phase DEA and DI ion yields and relative cross-sections for the potential FEBID precursor  $\text{CpFe}(\text{CO})_2\text{Mn}(\text{CO})_5$ , and we have used high-level coupled cluster calculations to aid the interpretation of our gas phase observations and to better understand the nature of the underlying negative ion states in DEA. Additionally, we report on the electron-induced dissociation of adsorbed  $\text{CpFe}(\text{CO})_2\text{Mn}(\text{CO})_5$  molecules and compare the nature of this process with the DEA and DI branching ratios observed in the gas phase. This specific molecule was studied for its bimetallic/heteronuclear architecture, as its FeMn metal core is considered to have potential for FEBID of functional alloy structures.

In summary, with regards to DEA to  $\text{CpFe}(\text{CO})_2\text{Mn}(\text{CO})_5$ , the dominant channels observed are single CO loss and cleavage of the Fe–Mn bond under  $[\text{Mn}(\text{CO})_5]^-$  formation, partly associated with a preceding single CO loss from the iron-containing moiety. Sequential CO loss from the molecular anion is also observed but to a much lesser extent than the two dominating channels. The average CO loss in these DEA processes is in the range from 0.6 to 1 CO unit per incident. For the metal–metal bond cleavage in DEA, charge retention is exclusively on the Mn-centred fragment; we rationalize that through quantum chemical calculations of the molecular orbital evolution during the dissociation process. The thermochemical thresholds, calculated at the DPLNO-CCSD(T) level of theory with aug-cc-pVTZ and aug-cc-pVQZ basis sets, agree well with our observations and allow a consistent interpretation of the experimental results. The persistence

of the pi-bound cyclopentadienyl ligand is similar to that previously observed for other polyhaptoligands<sup>19,64</sup> and we do not observe the quasi-continuous attachment profile recently reported for the high-performance heteronuclear FEBID precursor HFeCo<sub>3</sub>(CO)<sub>12</sub>.<sup>32,33</sup> On the contrary, we consider the electron attachment profile of CpFe(CO)<sub>2</sub>Mn(CO)<sub>5</sub> to be characterized by discrete resonances with insignificant overlap. With regards to DI, the predominant channels are the loss of 5 and 6 CO, the formation of [CpFe(CO)<sub>n</sub>]<sup>+</sup> with  $n = 0$  and 2 and the formation of the bare metal cations Fe<sup>+</sup> and Mn<sup>+</sup>. The fragmentation through DI is considerably more extensive than we observe through DEA, and we derive a lower limit of 3 and a higher limit of 6 for the average CO loss per incident through DI.

Electron-induced fragmentation of adsorbed CpFe(CO)<sub>2</sub>Mn(CO)<sub>5</sub> molecules is qualitatively in good agreement with the gas phase data, showing evidence of CO desorption but no indication of cyclopentadienyl group desorption. In the initial electron induced fragmentation of adsorbed CpFe(CO)<sub>2</sub>Mn(CO)<sub>5</sub> molecules an average of 5 CO molecules desorb. In direct comparison with the DI and DEA branching ratios observed in the gas phase, this suggests that DI-initiated deposition is dominant in the decomposition of CpFe(CO)<sub>2</sub>Mn(CO)<sub>5</sub> on the surface, rather than DEA.

We do not expect CpFe(CO)<sub>2</sub>Mn(CO)<sub>5</sub> to produce high metal content depositions in FEBID, largely due to the persistence of the cyclopentadienyl ligand both in the gas phase and on the surface. The likelihood of significant co-deposition of carbon from this ligand may require the use of post-deposition processing<sup>4,5</sup> in order to use this molecule as a precursor for the production of FeMn alloys via FEBID.

## Conflicts of interest

There are no conflicts to declare.

## Acknowledgements

This work was conducted under the support of the Icelandic Center of Research (RANNIS; Grants No. 13049305 and 141218051) and the University of Iceland Research Fund. The authors acknowledge the collaborative platform provided by the COST Action CM1301, CELINA and RMT acknowledges financial support for a STSM within CELINA. LM-W and DHF thank the US National Science Foundation for support through the linked collaborative grants CHE-1607547 and CHE-1607621.

## References

- J. M. De Teresa, A. Fernández-Pacheco, R. Córdoba, L. Serrano-Ramón, S. Sangiao and M. R. Ibarra, *J. Phys. D: Appl. Phys.*, 2016, **49**, 243003.
- J. Martín, J. Nogués, K. Liu, J. Vicent and I. K. Schuller, *J. Magn. Magn. Mater.*, 2003, **256**, 449–501.
- W. M. Kaminsky, G. A. C. Jones, N. K. Patel, W. E. Booiij, M. G. Blamire, S. M. Gardiner, Y. B. Xu and J. A. C. Bland, *Appl. Phys. Lett.*, 2001, **78**, 1589–1591.
- I. Utke, P. Hoffmann and J. Melngailis, *J. Vac. Sci. Technol., B: Microelectron. Nanometer Struct.–Process., Meas., Phenom.*, 2008, **26**, 1197–1276.
- W. F. van Dorp and C. W. Hagen, *J. Appl. Phys.*, 2008, **104**, 081301.
- W. F. van Dorp, B. van Someren, C. W. Hagen, P. Kruit and P. A. Crozier, *Nano Lett.*, 2005, **5**, 1303–1307.
- F. Porrati, M. Pohlit, J. Müller, S. Barth, F. Biegger, C. Gspan, H. Plank and M. Huth, *Nanotechnology*, 2015, **26**, 475701.
- L. Serrano-Ramón, R. Córdoba, L. A. Rodríguez, C. Magén, E. Snoeck, C. Gatel, I. Serrano, M. R. Ibarra and J. M. De Teresa, *ACS Nano*, 2011, **5**, 7781–7787.
- E. Begun, O. V. Dobrovolskiy, M. Kompaniits, R. Sachser, C. Gspan, H. Plank and M. Huth, *Nanotechnology*, 2015, **26**, 075301.
- R. Córdoba, D.-S. Han and B. Koopmans, *Microelectron. Eng.*, 2016, **153**, 60–65.
- R. M. Thorman, R. T. P. Kumar, D. H. Fairbrother and O. Ingólfsson, *Beilstein J. Nanotechnol.*, 2015, **6**, 1904–1926.
- J. Schaefer and J. Hoelzl, *Thin Solid Films*, 1972, **13**, 81–86.
- R. Schmied, J. D. Fowlkes, R. Winkler, P. D. Rack and H. Plank, *Beilstein J. Nanotechnol.*, 2015, **6**, 462–471.
- T. Verduin, S. Lokhorst, C. Hagen and P. Kruit, *Microelectron. Eng.*, 2016, **155**, 114–117.
- N. Silvis-Cividjian, C. Hagen, L. Leunissen and P. Kruit, *Microelectron. Eng.*, 2002, **61–62**, 693–699.
- P. C. Hoyle, J. R. A. Cleaver and H. Ahmed, *Appl. Phys. Lett.*, 1994, **64**, 1448–1450.
- S. G. Rosenberg, M. Barclay and D. H. Fairbrother, *J. Phys. Chem. C*, 2013, **117**, 16053–16064.
- S. G. Rosenberg, M. Barclay and D. H. Fairbrother, *Phys. Chem. Chem. Phys.*, 2013, **15**, 4002–4015.
- J. D. Wnuk, J. M. Gorham, S. G. Rosenberg, W. F. van Dorp, T. E. Madey, C. W. Hagen and D. H. Fairbrother, *J. Phys. Chem. C*, 2009, **113**, 2487–2496.
- S. Engmann, M. Stano, Š. Matejčík and O. Ingólfsson, *Phys. Chem. Chem. Phys.*, 2012, **14**, 14611–14618.
- S. Engmann, M. Stano, P. Papp, M. J. Brunger, Š. Matejčík and O. Ingólfsson, *J. Chem. Phys.*, 2013, **138**, 044305.
- O. May, D. Kubala and M. Allan, *Phys. Chem. Chem. Phys.*, 2012, **14**, 2979–2982.
- K. Wnorowski, M. Stano, C. Matias, S. Denifl, W. Barszczewska and Š. Matejčík, *Rapid Commun. Mass Spectrom.*, 2012, **26**, 2093–2098.
- O. Ingólfsson, F. Weik and E. Illenberger, *Int. J. Mass Spectrom. Ion Processes*, 1996, **155**, 1–68.
- I. Bald, J. Langer, P. Tegeder and O. Ingólfsson, *Int. J. Mass Spectrom.*, 2008, **277**, 4–25.
- E. Böhler, J. Warneke and P. Swiderek, *Chem. Soc. Rev.*, 2013, **42**, 9219–9231.
- L. G. Christophorou, *Electron-molecule interactions and their applications*, Academic Press, 1984.
- H. Hotop, M.-W. Ruf and I. Fabrikant, *Phys. Scr.*, 2004, **T110**, 22–31.
- C. R. Arumainayagam, H.-L. Lee, R. B. Nelson, D. R. Haines and R. P. Gunawardane, *Surf. Sci. Rep.*, 2010, **65**, 1–44.

- 30 I. I. Fabrikant, S. Eden, N. J. Mason and J. Fedor, *Adv. At., Mol., Opt. Phys.*, 2017, **66**, 545–657.
- 31 D. Klar, M.-W. Ruf and H. Hotop, *Int. J. Mass Spectrom.*, 2001, **205**, 93–110.
- 32 T. P. Ragesh Kumar, S. Barth, R. Bjornsson and O. Ingólfsson, *Eur. Phys. J. D*, 2016, **70**, 163.
- 33 T. P. Ragesh Kumar, R. Bjornsson, S. Barth and O. Ingólfsson, *Chem. Sci.*, 2017, **8**, 5949–5952.
- 34 M. Zlatar, M. Allan and J. Fedor, *J. Phys. Chem. C*, 2016, **120**, 10667–10674.
- 35 R. C. Che, M. Takeguchi, M. Shimojo, W. Zhang and K. Furuya, *Appl. Phys. Lett.*, 2005, **87**, 223109.
- 36 L. Bernau, M. Gabureac, R. Erni and I. Utke, *Angew. Chem., Int. Ed.*, 2010, **49**, 8880–8884.
- 37 F. Porrati, B. Kämpken, A. Terfort and M. Huth, *J. Appl. Phys.*, 2013, **113**, 053707.
- 38 T. P. Ragesh Kumar, I. Unlu, S. Barth, O. Ingólfsson and D. H. Fairbrother, *J. Phys. Chem. C*, 2017, DOI: 10.1021/acs.jpcc.7b08611.
- 39 T. P. Ragesh Kumar, P. Weirich, L. Hrachowina, M. Hanefeld, R. Bjornsson, H. R. Hrodmarsson, S. Barth, D. H. Fairbrother, M. Huth and O. Ingólfsson, *Beilstein J. Nanotechnol.*, 2017, accepted.
- 40 P. J. Hansen and R. A. Jacobson, *J. Organomet. Chem.*, 1966, **6**, 389–398.
- 41 E. H. Bjarnason, B. Ómarsson, S. Engmann, F. H. Ómarsson and O. Ingólfsson, *Eur. Phys. J. D*, 2014, **68**, 121.
- 42 F. Neese, *Wiley Interdiscip. Rev.: Comput. Mol. Sci.*, 2018, **8**, e1327.
- 43 A. D. Becke, *Phys. Rev. A: At., Mol., Opt. Phys.*, 1988, **38**, 3098–3100.
- 44 J. P. Perdew, *Phys. Rev. B: Condens. Matter Mater. Phys.*, 1986, **33**, 8822–8824.
- 45 F. Weigend and R. Ahlrichs, *Phys. Chem. Chem. Phys.*, 2005, **7**, 3297.
- 46 S. Grimme, J. Antony, S. Ehrlich and H. Krieg, *J. Chem. Phys.*, 2010, **132**, 154104.
- 47 S. Grimme, S. Ehrlich and L. Goerigk, *J. Comput. Chem.*, 2011, **32**, 1456–1465.
- 48 C. Riplinger and F. Neese, *J. Chem. Phys.*, 2013, **138**, 034106.
- 49 C. Riplinger, B. Sandhoefer, A. Hansen and F. Neese, *J. Chem. Phys.*, 2013, **139**, 134101.
- 50 C. Riplinger, P. Pinski, U. Becker, E. F. Valeev and F. Neese, *J. Chem. Phys.*, 2016, **144**, 024109.
- 51 M. Saitow, U. Becker, C. Riplinger, E. F. Valeev and F. Neese, *J. Chem. Phys.*, 2017, **146**, 164105.
- 52 T. H. Dunning, *J. Chem. Phys.*, 1989, **90**, 1007–1023.
- 53 N. B. Balabanov and K. A. Peterson, *J. Chem. Phys.*, 2005, **123**, 064107.
- 54 F. Neese, *J. Am. Chem. Soc.*, 2006, **128**, 10213–10222.
- 55 G. Knizia, *J. Chem. Theory Comput.*, 2013, **9**, 4834–4843.
- 56 I. Mayer, *Chem. Phys. Lett.*, 1983, **97**, 270–274.
- 57 I. Mayer, *Int. J. Quantum Chem.*, 1984, **26**, 151–154.
- 58 I. Mayer, *Theor. Chim. Acta*, 1985, **67**, 315–322.
- 59 I. Mayer, On the chemical Hamiltonian approach, bond orders and valences, *Modelling of Structure and Properties of Molecules*, Ellis Horwood, Chichester, 1987.
- 60 R. M. Thorman, R. Bjornsson and O. Ingólfsson, *Eur. Phys. J. D*, 2016, **70**, 164.
- 61 R. M. Thorman, J. A. Brannaka, L. McElwee-White and O. Ingólfsson, *Phys. Chem. Chem. Phys.*, 2017, **19**, 13264–13271.
- 62 X. Feng, N. Li, L. Lv and R. B. King, *New J. Chem.*, 2016, **40**, 7482–7492.
- 63 I. Unlu, J. Spencer, K. Johnson, R. Thorman, O. Ingólfsson, L. McElwee-White and D. H. Fairbrother, 2017, submitted.
- 64 J. A. Spencer, J. A. Brannaka, M. Barclay, L. McElwee-White and D. H. Fairbrother, *J. Phys. Chem. C*, 2015, **119**, 15349–15359.
- 65 M. Barber, J. A. Connor, M. F. Guest, M. B. Hall, I. H. Hillier and W. N. E. Meredith, *Faraday Discuss. Chem. Soc.*, 1972, **54**, 219–226.
- 66 E. W. Plummer, W. R. Salaneck and J. S. Miller, *Phys. Rev. B: Solid State*, 1978, **18**, 1673–1701.
- 67 J. A. Spencer, Y.-C. Wu, L. McElwee-White and D. H. Fairbrother, *J. Am. Chem. Soc.*, 2016, **138**, 9172–9182.
- 68 J. Lengyel, P. Papp, Š. Matejčík, J. Kočíšek, M. Fárnik and J. Fedor, *Beilstein J. Nanotechnol.*, 2017, **8**, 2200–2207.